A3COSMOS: the dust attenuation of star-forming galaxies at $z = 2.5$–4.0 from the COSMOS-ALMA archive

Yoshinobu Fudamoto [1]⋆ P. A. Oesch [1,2] B. Magnelli [3] E. Schinnerer [4] D. Liu [4]
P. Lang,[4] E. F. Jiménez-Andrade [3] B. Groves,[5] S. Leslie [4] and M. T. Sargent [6]

[1]*Department of Astronomy, University of Geneva, 51 Ch. des Maillettes, 1290 Versoix, Switzerland*
[2]*International Associate, Cosmic Dawn Center (DAWN), 2100 Copenhagen, Denmark*
[3]*Argelander-Institut für Astronomie, Universität Bonn, Auf dem Hügel 71, D-53121 Bonn, Germany*
[4]*Max Planck Institute for Astronomy, Königstuhl 17, D-69117 Heidelberg, Germany*
[5]*Research School of Astronomy & Astrophysics, Australian National University, Mt. Stromlo Observatory, Cotter Rd, Weston Creek, ACT 2611, Australia*
[6]*Astronomy Centre, Department of Physics and Astronomy, University of Sussex, Brighton BN1 9QH, UK*

ABSTRACT

We present an analysis of the dust attenuation of star-forming galaxies at $z = 2.5$–4.0 through the relationship between the UV spectral slope (β), stellar mass (M_*), and the infrared excess (IRX $= L_{IR}/L_{UV}$) based on far-infrared continuum observations from the Atacama Large Millimeter/sub-millimeter Array (ALMA). Our study exploits the full ALMA archive over the COSMOS field processed by the A3COSMOS team, which includes an unprecedented sample of $\sim$1500 galaxies at $z \sim 3$ as primary or secondary targets in ALMA band 6 or 7 observations with a median continuum sensitivity of 126 µJy beam^{-1} (1σ). The detection rate is highly mass dependent, decreasing drastically below $\log(M_*/M_\odot) = 10.5$. The detected galaxies show that the IRX–β relationship of massive ($\log M_*/M_\odot > 10$) main-sequence galaxies at $z = 2.5$–4.0 is consistent with that of local galaxies, while starbursts are generally offset by ~ 0.5 dex to larger IRX values. At the low-mass end, we derive upper limits on the infrared luminosities through stacking of the ALMA data. The combined IRX–M_* relation at $\log(M_*/M_\odot) > 9$ exhibits a significantly steeper slope than reported in previous studies at similar redshifts, implying little dust obscuration at $\log M_*/M_\odot < 10$. However, our results are consistent with earlier measurements at $z \sim 5.5$, indicating a potential redshift evolution between $z \sim 2$ and $z \sim 6$. Deeper observations targeting low-mass galaxies will be required to confirm this finding.

Key words: galaxies: evolution – galaxies: ISM – galaxies: star formation – submillimetre: ISM.

1 INTRODUCTION

The total census of the star formation rate density (SFRD) of galaxies across cosmological time is a major milestone of modern extragalactic research (e.g. review by Madau & Dickinson 2014, and references therein). Deep rest-frame ultraviolet (UV) photometry obtained by the *Hubble Space Telescope* (*HST*), especially after the advent of the Wide Field Camera (WFC3) has now collected large galaxy samples at $z \sim 7$–8, and has even pushed the measurement of the SFRD to $z > 10$ (Ellis et al. 2013; McLure et al. 2013; Schenker et al. 2013; Bouwens et al. 2014; Finkelstein et al. 2015; Kawamata et al. 2015; Oesch et al. 2015, 2018; Laporte et al. 2016; McLeod, McLure & Dunlop 2016). However, *HST* provides a very biased view of high-redshift galaxies, in particular at $z > 3$ where

it only has access to the rest-frame UV. The UV emission is highly sensitive to absorption by interstellar dust. The absorbed energy is re-emitted as thermal emission at far-infrared (FIR) wavelengths, and dominates the galaxies' bolometric energy output until redshift $z \sim 2$, and contributes significantly out to even higher redshift (Le Borgne et al. 2009; Magdis et al. 2012; Magnelli et al. 2013; Béthermin et al. 2015; Casey et al. 2018a; Zavala et al. 2018). Thus, the understanding of the dust extinction and re-emission in various environments and at different redshifts is a crucial ingredient in studying the star formation activity of galaxies, in particular in the high-redshift Universe.

The empirical relation between the infrared excess ($= L_{IR}/L_{UV}$; hereafter IRX), and UV spectral slope (β; $f_\lambda(\lambda) \propto \lambda^\beta$) is the most commonly used tool to derive a correction for dust attenuation (Meurer, Heckman & Calzetti 1999; Gordon et al. 2000). In the local Universe, studies find starburst galaxies to follow a relatively tight relationship in the IRX–β diagrams (Meurer et al. 1999; Takeuchi

⋆ E-mail: yoshinobu.fudamoto@unige.ch

et al. 2010; Overzier et al. 2011). In particular, Meurer et al. (1999, hereafter M99) derived the IRX–β relation using a sample of compact starburst galaxies observed by the *International Ultraviolet Explorer* (*IUE*; Kinney et al. 1993), and FIR flux measurements from the *Infrared Astronomical Satellite*. The M99 relation is applied to estimate the dust attenuation over virtually the entire redshift range of galaxies, with the assumption that high-redshift young galaxies share similar characteristics with local starburst galaxies.

However, even in the local Universe, the IRX relation presented by M99 has been extensively revised by several studies. Remeasurements of the M99 galaxies with the *Galaxy Evolution Explorer* (GALEX) reveal that a large part of the UV fluxes were previously underestimated due to the small aperture of *IUE*, and this biases the M99 relation towards higher IRX at fixed β (Overzier et al. 2011; Takeuchi et al. 2012). Also, it is highly debated if the IRX–β relation is universally applicable to local non-starburst galaxies. While some studies find that the general galaxy population follows a relatively tight IRX–β relation (Casey et al. 2014; Salim & Boquien 2018), other studies find significant scatter due to the contribution from older stellar populations, and offsets that might be correlated with stellar population ages (Kong et al. 2004; Buat et al. 2005; Grasha et al. 2013).

At higher redshift, the situation is even less clear. Using IR observations from *Spitzer*/MIPS, early studies have found that an IRX–β relation consistent with M99 is already established at redshift up to $z \sim 2.5$, although with significant scatter (Reddy et al. 2010, 2012; Whitaker et al. 2012). Using deep ALMA observations, Bouwens et al. (2016) showed that the M99 relation is not applicable for $z > 2$ less massive galaxies with $M_* < 10^{9.75} \, M_\odot$, and a steeper, SMC-like dust extinction curve is required to explain the low observed infrared fluxes of galaxies in the HUDF. On the other hand, several studies find that the M99 relation does still hold for $z \sim 2$–3 galaxies on the main sequence (Álvarez-Márquez et al. 2016; Fudamoto et al. 2017; McLure et al. 2018). Capak et al. (2015) and Faisst et al. (2017) show that, for $z \sim 5.5$ galaxies, the IRX is much lower than the M99 relation unless one assumes a significantly higher dust temperature ($T_d > 50 \, K$).

The correlations between IR luminosity and other physical properties, in addition to β, have also been investigated. Studies show that the IRX is also strongly correlated with stellar mass (M_*) (Heinis et al. 2014; Pannella et al. 2015; Álvarez-Márquez et al. 2016, 2019; Dunlop et al. 2017; Koprowski et al. 2018; Qin et al. 2019). This is not surprising, as the stellar mass of a galaxy reflects its past star-forming activity, and is a priori an indicator of the dustiness of the interstellar material as the dust particles are produced through stellar activity such as pulsating moderate mass stars and supernovae (e.g. Scalo & Slavsky 1980).

One major shortcoming of many previous studies was that they had to rely on *stacking* of low-resolution images, e.g. from *Herschel*, to infer the average infrared luminosity of a sample of galaxies, which is significantly affected by foreground contamination and clustered, neighbouring objects. While stacking analyses can reveal the average properties, they lose important information such as the scatter in the population. Thus, it is still unclear if there is a large scatter in the IRX relations and/or if there is a fraction of galaxies that are significantly offset from the average relations. The only way to resolve previous discrepancies are higher resolution FIR continuum measurements of individual galaxies to study the scatter in the IRX–β/M_* relation at high redshifts. This has become possible after the developments of sensitive/high-resolution millimetre or sub-millimetre observing facilities such as the Atacama

Large Millimeter/submillimeter Array (ALMA) and the Northern Extended Millimeter Array (NOEMA).

Using these facilities, the IRX–β/M_* of high-redshift star-forming galaxies is now routinely studied, yet important open questions remain. In our previous study (Fudamoto et al. 2017), we use ALMA band 6 observations of massive ($\log M_*/M_\odot > 10.5$) star-forming galaxies to show that massive galaxies at $z \sim 3$ generally follow the local relation. However, the sample size (~ 60 galaxies) and the dynamic range of β/M_* covered were small, limiting the conclusions.

In this paper, we update our previous studies on the IRX–β and the IRX–M_* relationship of star-forming galaxies at $z = 2.5$–4.0, using individual FIR flux measurements for 1512 galaxies (of which ~ 10 per cent are $>3\sigma$ detections) obtained from public ALMA archival data over the 2 deg^2 Cosmic Evolution Survey field (COSMOS; Koekemoer et al. 2007; Scoville et al. 2007), in order to provide new insight into the dust attenuation of high-redshift galaxies. The paper is organized as follows. In Section 2, we describe our sample and galaxy selection, and Section 3 presents the method of our analysis. Section 4 shows the results on the IRX–β/M_* relation obtained from our sample, and we conclude our study in Section 5.

Throughout this paper, we assume a cosmology with (Ω_m, Ω_λ, h_0) = (0.3, 0.7, 0.7) and a Chabrier IMF (Chabrier 2003). When comparing to previous measurements in the literature with a Salpeter (1955) IMF, we divide masses, $M_{*,Salpeter}$, by 1.58 (Ilbert et al. 2010; Madau & Dickinson 2014), and SFR$_{Salpeter}$ by 1.78 (Salim et al. 2007) to convert to a Chabrier IMF.

2 DATA AND SAMPLE SELECTION

In this section, we present our sample obtained from the public ALMA archive in the COSMOS field. All the steps of our data acquisition, imaging, source extraction, and FIR continuum photometry are fully described in our data release paper (A3COSMOS;[1] Liu et al. 2019), and interested readers are referred to it for more detail. Below, we only provide a brief summary.

2.1 A3COSMOS prior photometry data based on the COSMOS2015 catalogue

We made use of all the ALMA archival band 6 and band 7 observations in the COSMOS field that were publicly available as of January 2018. After obtaining the raw data from the ALMA archive, all the data are calibrated using the script released by the QA2 analyst for each PI project (i.e. scriptForPI.py). These scripts use the Common Astronomy Software Applications (CASA) package (McMullin et al. 2007). In particular, we used the appropriate version of CASA as specified by the scripts. The calibrated visibility data are then imaged and deconvolved from their dirty beam with the CLEAN algorithm of the imaging pipeline using a Briggs weighting scheme with a stopping threshold of S/N = 4 and a robustness parameter of 2 (i.e. natural weighting), and spatial extent up to a primary beam attenuation of 0.2. Projects for which the imaging pipeline failed were instead imaged manually by using a consistent weight and a spatial extent.

The ALMA photometry relies on a prior source extraction. We only selected galaxies that have counterparts in the deep optical to near-infrared photometry catalogue of the COSMOS field (hereafter

---

[1]https://sites.google.com/view/a3cosmos

COSMOS2015: Laigle et al. [2016](). The COSMOS2015 catalogue
is based on the source extraction on a combined NIR image from
the UltraVISTA survey (*J, H, K* bands; McCracken et al. [2012]()), and
the z^{++} image from the Subaru telescope.

The photometry from the ALMA images is obtained using GALFIT
(Peng [2002](); Peng et al. [2010]()) on the de-convolved image, which
results in accurate total flux measurements even for sources that
are marginally resolved. The flux measurement errors are estimated
based on fitting errors of the 2D Gaussian fits to the sources ac-
cording to Condon ([1997]()). Data release 1 of A3COSMOS contains
continuum observations of 1544 ALMA pointings, covering a total
of ~ 243 arcmin. We excluded all objects outside of the half primary
beam-width of each image. Additionally, we only include images
that have a resulting synthesized beam minor axis of >0.5 arcsec in
order to avoid that the sources are significantly resolved and fluxes
are missed.

The data sets that we include have resulting synthesized beam
sizes of 0.5–1.8 arcsec with median beam size of 1.1 arcsec, and
the median continuum sensitivity has an rms of 126 μJy beam^{-1}
with standard deviation of a 91 μJy beam^{-1}, after applying primary
beam corrections.

2.2 Star-forming galaxy sample selection

Starting from the full A3COSMOS data set, we select all ALMA
pointings that contain a galaxy at $z = 2.5$–4.0, using the photometric
redshifts from the COSMOS2015 catalogue. In particular, we only
select galaxies with accurately determined photometric redshifts,
$\delta_{z_{ph}}/(1 + z_{ph}) < 0.2$, where $\delta_{z_{ph}}$ corresponds to the 16–84th per-
centile width of the z_{ph} estimation in the COSMOS2015 catalogue.

Stellar masses are also taken from the COSMOS2015 catalogue,
which have been estimated using the LePhare SED-fitting code
(Arnouts et al. [2002](); Ilbert et al. [2006]()) with stellar population syn-
thesis models of Bruzual & Charlot ([2003]()) combining exponentially
declining and delayed star formation histories (SFHs). Solar and half
solar metallicities are considered. The median of the marginalized
probability distribution function (PDF) is used throughout this paper
(mass_med column in the COSMOS2015 catalogue), and 16th, 84th
percentile of the PDF is used as an estimate of the mass uncertainty.

Active galactic nuclei (AGNs) could potentially affect our analy-
sis, as massive galaxies are frequently identified as hosts of AGNs.
Although the contribution of AGN emission is small in the FIR
wavebands (e.g. Hatziminaoglou et al. [2010](); Béthermin et al. [2015]()),
an AGN could outshine or significantly contribute to the rest-frame
UV emission of its host galaxy, which would significantly affect the
UV slope measurement.

To restrict our sample to star forming galaxies, we adopt the
following additional selection criteria:

(1) The X-ray detected galaxies are identified as un-obscured
AGNs. Thus, we exclude galaxies that have counterparts in the
deep Chandra X-ray catalogue of Civano et al. ([2016]()). We cross-
correlated our sample with the catalogue using a matching radius
of 1.5 arcsec. 46 of our sources have a clear X-ray detection and are
thus excluded from further analysis.

(2) We further exclude potential AGNs through the rest-frame
mid-infrared (MIR) photometry from *Spitzer* IRAC. We employ
MIR-AGN selection criteria developed by Donley et al. ([2012]()),
which incorporate rest-frame mid-infrared colours to select ob-
scured AGNs. This method efficiently selects Compton-thick AGNs
through their AGN-heated dust colours in their rest-frame MIR
wavebands. The MIR colour selection successfully avoids selecting

moderate- to high-redshift normal star-forming galaxies at $z \sim 0.5$–3
as AGNs. This selection excludes only 44 sources from our sample.

Our final sample then includes 1512 galaxies at $z = 2.5$–4.0
with median redshift $z_{ph} = 2.95$, and median stellar mass $\log M_* =$
9.82 M$_\odot$. 172 galaxies out of this sample are detected at more than
3σ with ALMA and 1338 only have upper limits.

3 ANALYSIS

Among our final sample, the FIR detections are constrained to
massive ($M_* \gtrsim 10^{10}$ M$_\odot$) galaxies only (Fig. [1]()). Below this, most
galaxies do not show significant dust continuum emission, down
to the limits of current ALMA data sets in COSMOS. This is
consistent with previous findings (e.g. Dunlop et al. [2017](); Bouwens
et al. [2016]()). The mass distribution of our input catalogue peaks
at $M_* \sim 10^{9.5}$ M$_\odot$. Fainter low-mass galaxies with $M_* \lesssim 10^{9.0}$ M$_\odot$
are generally not included due to their larger photometric redshift
uncertainties.

3.1 Total SFR estimation of ALMA-detected sources

Interstellar dust absorbs UV emission from O-, B-type stars, and
re-emits the energy at FIR wavelengths. A total measure of star
formation rate (SFR$_{tot}$) can be obtained by combining UV and IR
luminosities of galaxies that are detected in FIR observations. For
the ALMA detected sample at $z_{ph} = 2.5$–4.0, we thus calculate star
formation rates (SFRs) by employing the equations from Kennicutt
([1998]()) to the L_{IR} and L_{UV} estimated in Section 3.2 and 3.3. The
SFRs from attenuation uncorrected UV luminosities (SFR$_{UV}$) are
calculated as

$$\text{SFR}_{UV}\,(M_*\,\text{yr}^{-1}) = 0.79 \times 10^{-28}\,L_{\nu_{1600}}\,(\text{erg s}^{-1}\,\text{Hz}^{-1}), \quad (1)$$

at $\lambda = 1600$ Å, and the SFRs estimated from the IR luminosities
(SFR$_{IR}$) are calculated as

$$\text{SFR}_{IR}\,(M_*\,\text{yr}^{-1}) = 2.53 \times 10^{-44}\,L_{IR}\,(\text{erg s}^{-1}), \quad (2)$$

where L_{IR} is the FIR luminosity integrated over $\lambda = 8$–1000 μm.
The total SFR (SFR$_{tot}$) of the sample is then defined as SFR$_{tot} =$
SFR$_{UV}$ + SFR$_{IR}$. For ALMA non-detected galaxies, we directly use
the SFR estimation from the COSMOS2015 catalogue as the total
SFR of the galaxies, which is based on SED fitting employing a
Calzetti extinction curve. In the right-hand panel of Fig. [1](), we show
the SFR–M_* diagram of our sample. ALMA detected galaxies and
non-detected galaxies together form a tight relation between stellar
mass and SFR, which is known as the main sequence of star-forming
galaxies (e.g. Daddi et al. [2007](); Elbaz et al. [2007](); Noeske et al. [2007]();
Peng et al. [2010]()).

3.2 L_{IR} estimation

The IR luminosities, L_{IR}, of our galaxies are estimated from the
ALMA continuum fluxes. For this, we use the integrated flux on
the cleaned images described in Section 2. L_{IR} is then estimated
by scaling an SED template to the measured flux in ALMA band
6 $\lambda \sim 1100$–1400 μm or ALMA band 7 $\lambda \sim 800$–1100 μm. In
particular, we use the empirical SED template that was previously
derived for $z \sim 3$ galaxies by Álvarez-Márquez et al. ([2016]()). This
template is based on the SED library of Dale et al. ([2014]()), and
is obtained by fitting stacked fluxes over a wide range of wave-
lengths (100–1100 μm). Álvarez-Márquez et al. ([2016]()) perform
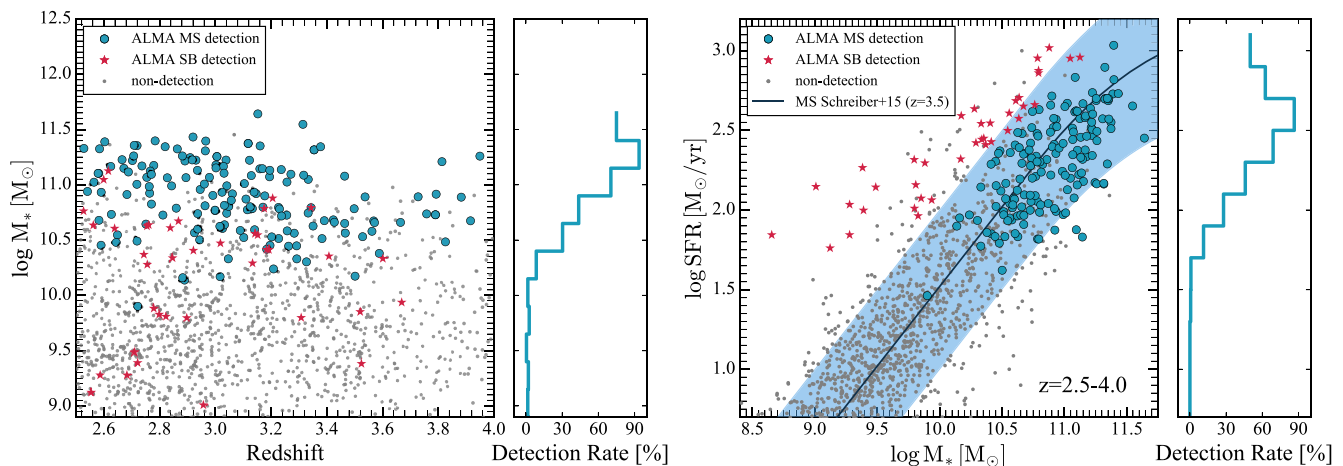their stacking analyses for 22 000 galaxies selected by a Lyman

Figure 1. *Left:* The distribution of our sample in stellar mass (M_*) versus photometric redshift (z_{ph}). *Right:* The star formation rate (SFR) and stellar mass diagram showing the main-sequence of galaxies at $z = 2.5$–4.0. The solid line represents the main-sequence at $z = 3.5$ measured in Schreiber et al. (2015), and the blue band indicates ± 0.5 dex from the relation (see Section 3.4 for more details). For both panels, blue points and red stars indicate our main-sequence (MS) and starburst (SB) galaxies sample detected in ALMA band 6 or band 7 ($> 3\sigma$ signal at the prior position), respectively. Starbursts are defined as galaxies with SFRs $3\times$ above the main-sequence at their redshift. Grey dots show the sample that lies within the ALMA field of view (i.e. within half primary beamwidth), but did not yield a detection. For FIR detected galaxies, the total SFR is calculated from both L_{UV} and L_{IR} (see Section 3.1). For non-detected sources, SFRs are obtained from SED fitting to the optical to near-infrared photometry in the COSMOS2015 catalogue. Most FIR detections are concentrated at the massive ($M_* \gtrsim 10^{10}\,M_\odot$) end of the original catalogue.

break technique as a function of L_{UV}, β, and M_* after correcting the IR fluxes for clustering of galaxies and catalogue incompleteness. From their results, we use, in particular, the SED template obtained in the mass range of $\log M_*/M_\odot = 10.25$–10.75, for which they find $\alpha_{dale} = 1.7$ in the Dale et al. (2014) description. As shown in the Appendix, this SED is also a good match to the average stacked *Herschel* FIR fluxes of our sample, and is thus an appropriate choice to estimate the total IR luminosities.

We redshift this SED template to the z_{ph} of each galaxy and rescale it to the measured ALMA flux. L_{IR} is then calculated by integrating the SED template over the rest-frame wavelength range 8–1000 μm. Uncertainties on L_{IR} are estimated by propagating the flux measurement uncertainties. For galaxies that are not detected in ALMA, we estimate the 3σ L_{IR} upper limit based on the image rms, assuming the galaxies are not significantly resolved in the ALMA data, which have a resolution cut of >0.5 arcsec (see Section 2.1).

Clearly, the exact values of L_{IR} depend on the assumed SED template, which we discuss in more detail in the Appendix. Using a wide range of templates, we find a systematic spread of ± 0.2 dex on L_{IR}, around the value derived with our baseline template. We therefore include this systematic uncertainty in addition to the measurement uncertainties when we report L_{IR} values. Note, however, that the choice of a specific SED template as tested in the appendix does not affect our main conclusions.

3.3 L_{UV} and β measurements

The UV spectral slopes (β) of our sample are estimated by employing SED fitting to photometric data from the COSMOS2015 catalogue, including broad-, intermediate-, and narrow-band filter observations at optical to NIR wavelengths after applying offsets and foreground extinction corrections following the description in the appendix A.2 of Laigle et al. (2016). The photometry is then fitted using the code ZEBRA + in combination with stellar synthesis templates based on Bruzual & Charlot (2003) of varying SFHs and metallicities, to which we added emission lines and nebular

continuum emission (see Oesch et al. 2010). To keep our results unbiased, we assumed two sets of extinction curves of local star-forming galaxies (Calzetti 2001) and that measured for the SMC (Gordon et al. 2003).

For each SED model, we calculate β over the wavelength range of $1500 < \lambda < 2500$ Å, and we derive a marginalized probability distribution function of β for each individual galaxy based on the χ^2 values of each template. From this, we compute the median β value and its uncertainties based on the 16th and 84th percentiles. Similarly, the monochromatic UV luminosities are calculated from the best fit SEDs at 1600 Å, with respective uncertainties, where we define $L_{UV} = \nu_{1600} L_{\nu_{1600}}$.

Fig. 2 shows the β estimations against stellar mass. We fit the relation with a third-order polynomial function to the error weighted individual data points resulting in the following:

$$\beta = -1.17\,(\pm 0.01) + 0.63\,(\pm 0.03)\,X \\ + 0.22\,(\pm 0.02)\,X^2 + 0.11\,(\pm 0.02)\,X^3, \tag{3}$$

where $X = \log(M_*/10^{10}\,M_\odot)$. As shown in the Fig. 2, this relation is in excellent agreement with McLure et al. (2018), who used a complete galaxy sample from all prime extragalactic legacy fields (HUDF, CANDELS, GOODS-S, CANDELS UDS, and the UVISTA survey). This indicates that our sample, selected within ALMA pointings, is not biased in its UV slope distribution as a function of stellar mass.

3.4 Classifying galaxies as main-sequence galaxies or starbursts

In order to study how starburst galaxies affect the IRX–β relationship, we classified our sample either as starburst or main-sequence galaxies using our best estimate of their SFR (i.e. SFR$_{tot}$ for the FIR continuum detected galaxies, or SFR$_{SED}$ for ALMA non-detections). The main-sequence (MS) relation as a function of redshift is taken from Schreiber et al. (2015), and we defined galaxies as starbursts when they have SFR three times larger
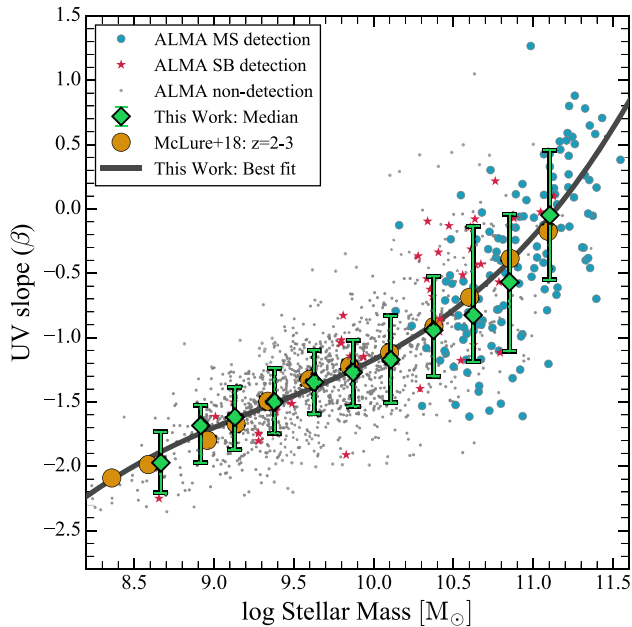
Figure 2. Observed UV slope (β) against stellar mass of our sample. Blue, red stars, and grey dots show individual galaxy measurement corresponding to ALMA-detected main-sequence (MS) galaxies, ALMA-detected starbursts (SB), and non-detections, respectively. The blue diamonds show median UV continuum slopes β, binned by stellar mass ($\Delta M_* = 0.25$ dex), and the error bars show the 16th and 84th percentiles, indicating the distribution of β in each bin. The black solid line shows our error weighted fit to the individual data points using a cubic polynomial function. Large yellow points show the results from McLure et al. (2018), who use a sample of star-forming galaxies at $z = 2$–3 observed in the HUDF, CANDELS GOODS-S, CANDELS UDS, and UVISTA surveys. McLure et al. (2018) and our study give essentially identical results on the β–M_* relation, which assures us that our sample selected from a wider area data set has a properly sampled β distribution.

than the MS at their photometric redshift. The FIR continuum detected sample as well as non-detected galaxies form a tight relation in the diagram following the main-sequence found in Schreiber et al. (2015). 228 galaxies in our sample are classified as starbursts. In the following, we will discuss SBs and MS galaxies separately.

3.5 Stacking analysis

Although only ~ 10 per cent of our full sample is detected with ALMA at $> 3\sigma$ significance, the average ALMA fluxes including both detected and non-detected galaxies carry important information, which is why we perform a stacking analysis. The main difficulty we have to overcome is that our data set includes images from different projects with varying beam sizes/orientations. Hence, an image stack is not straightforward. After testing different methods, we decided to opt for the simplest solution and to follow McLure et al. (2018), who derive average IRX measurements for different bins of galaxy masses and UV continuum slopes by stacking the ALMA aperture flux measurements. We compare these flux stacks to image stacks for a sub-sample of spectroscopically confirmed galaxies in Section 4.2.1.

For our stacking method, we first need an ALMA flux measurement for each galaxy. Since the A3COSMOS catalogue only provides fluxes for detections, we work with the ALMA continuum

images directly, and derive our own flux measurements. We measure the ALMA flux of each galaxy within an aperture with a fixed radius of 2 arcsec. A small aperture correction is then applied, dividing these fluxes by the dirty beam area within this aperture. The fixed aperture radius was chosen to best reproduce the total flux measurements of individually detected sources in the A3COSMOS catalogue.

For galaxies with $> 3\sigma$ detections in the A3COSMOS catalogue, we perform these measurements on the dirty images, while for undetected sources, we perform these measurements on the clean images. This ensures that in both cases the signal corresponds to a dirty beam, and that sidelobes from bright sources within the same image do not affect our measurements. The weights for the stacks are based on the rms values that are corrected by primary beam attenuation at the positions of objects.

The results of our stacking analyses are listed in Table 1 and will be discussed in the following sections.

4 RESULTS

4.1 The IRX–β relation at $z = 2.5$–4.0

In the following sections, we first analyse the IRX–β relation by separating our sample at a threshold stellar mass above and below $M_* = 10^{10}\,\mathrm{M_\odot}$.

4.1.1 IRX–β relation of massive galaxies ($M_* > 10^{10}\,\mathrm{M_\odot}$)

The left-hand panel of Fig. 3 shows the IRX–β relation of the massive galaxies. Our sample covers a wide range of $\beta \sim -1.5$–1.0, which is very close to the range originally sampled by M99. Individually detected galaxies show a fairly tight IRX–β relation, consistent with that of local starburst galaxies.

In order to compute the average IRX of the whole population (not only of ALMA detections), we performed a stacking analysis on the full main-sequence galaxy sample, as described in Section 3.5. The mean stacked IRX measurements in bins of β almost perfectly follow the local relation of M99 (Fig. 3). This is consistent with our pilot study (Fudamoto et al. 2017), and with several previous studies employing stacking analyses (e.g. Álvarez-Márquez et al. 2016; Koprowski et al. 2018).

Our L_{IR} estimation could vary by up to ~ 0.2 dex when applying different SED models (see the Appendix). Given this uncertainty, we cannot conclusively distinguish between the original M99 relation or its updated version (Overzier et al. 2011) for our massive galaxy sample. However, we can clearly rule out the SMC relation for these galaxies, as the systematic uncertainties due to the SEDs are much smaller than the difference between the SMC and the M99 relation.

The observed IRX–β relation is relatively tight. The random scatter around the mean relation is only $\sigma_{\mathrm{IRX}} \sim 0.27$ dex (excluding the systematic uncertainty due to the IR SED). This value is significantly smaller than the ~ 0.5 dex reported in Fudamoto et al. (2017). The much larger statistics clearly improved our measurement. Additionally, our previous UV continuum slopes were derived from power-law fits to the photometry rather than using properly sampled UV slopes probability distributions from SED fitting.

Individually, most of the 3σ upper limits from the non-detected, massive galaxies are consistent with random scatter. Given our detection limits, only three galaxies lie more than $3 \times \sigma_{\mathrm{IRX}}$ below the M99 relation. From UV observations, these galaxies do not

Table 1. Results of the stacking analysis.

Range	Number of sources	$\langle z \rangle$	$\langle \beta \rangle$	log $\langle L_{UV} \rangle$ (L$_\odot$)	log $\langle M_* \rangle$ (M$_\odot$)	logL_{IR} (L$_\odot$)	logIRX
			Stack in bins of β at log $M_*/M_\odot > 10$				
$-2.2 < \beta < -1.5$	26	3.31 ± 0.32	-1.58 ± 0.11	10.91 ± 0.20	10.13 ± 0.25	11.84 ± 0.22	0.89 ± 0.26
$-1.5 < \beta < -1.0$	121	3.19 ± 0.34	-1.20 ± 0.14	10.75 ± 0.30	10.26 ± 0.24	11.44 ± 0.23	0.64 ± 0.32
$-1.0 < \beta < -0.5$	131	3.14 ± 0.36	-0.82 ± 0.13	10.53 ± 0.44	10.44 ± 0.29	11.85 ± 0.21	1.40 ± 0.27
$-0.5 < \beta < 0.0$	72	2.96 ± 0.37	-0.24 ± 0.14	10.18 ± 0.29	10.74 ± 0.31	12.11 ± 0.21	1.89 ± 0.26
$0.0 < \beta < 0.5$	27	2.93 ± 0.27	0.25 ± 0.13	9.95 ± 0.19	11.09 ± 0.32	12.42 ± 0.21	2.46 ± 0.27
$0.5 < \beta < 1.0$	12	2.90 ± 0.09	0.68 ± 0.16	9.93 ± 0.19	11.25 ± 0.01	12.51 ± 0.21	2.70 ± 0.28
			Stack in bins of β at log $M_*/M_\odot = 9$–10				
$-2.2 < \beta < -1.5$	239	3.12 ± 0.40	-1.67 ± 0.15	10.30 ± 0.28	9.34 ± 0.25	<10.68	<0.58
$-1.5 < \beta$	353	3.01 ± 0.36	-1.29 ± 0.19	10.33 ± 0.26	9.63 ± 0.23	<10.51	<0.28
			Stack in bins of log M_*				
$11.0 < M_* < 12.0$	51	3.20 ± 0.17	-0.06 ± 0.65	10.26 ± 0.34	11.15 ± 0.17	12.45 ± 0.21	2.30 ± 0.23
$10.5 < M_* < 11.0$	132	3.28 ± 0.26	-0.84 ± 0.45	10.64 ± 0.38	10.68 ± 0.13	11.98 ± 0.22	1.33 ± 0.23
$10.0 < M_* < 10.5$	212	3.34 ± 0.25	-1.10 ± 0.34	10.71 ± 0.32	10.23 ± 0.15	11.36 ± 0.26	0.75 ± 0.29
$9.5 < M_* < 10.0$	318	3.40 ± 0.26	-1.36 ± 0.24	10.46 ± 0.24	9.72 ± 0.14	<10.53	<0.19
			Stack of spec-z sample				
$9.5 < M_* < 10.0$	61	3.44 ± 0.41	-1.23 ± 0.26	10.94 ± 0.22	10.08 ± 0.20	11.13 ± 0.26	0.24 ± 0.27

Note. The parentheses $\langle \rangle$ represent median values of the stacked sample, and the uncertainty correspond to standard deviations.
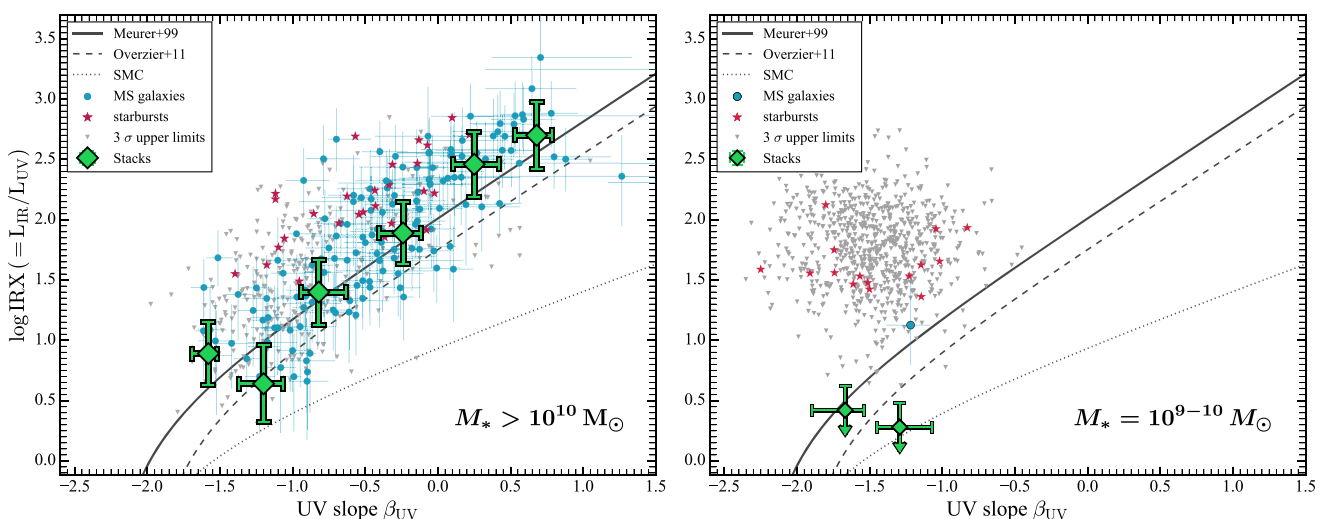

Figure 3. IRX–β diagram of massive ($M_* > 10^{10}$ M$_\odot$, *left*) and less massive (10^9 M$_\odot < M_* < 10^{10}$ M$_\odot$, *right*) galaxies at $z \sim 2.5$–4.0. Blue points are individual FIR continuum detections of main-sequence galaxies (with significance $> 3\sigma$). Red stars indicate the FIR continuum detected starburst galaxies (see Section 3.4). Grey triangles show 3σ upper limits for non-detected sources. Large green diamonds are results from a stacking analysis of the main-sequence sample. The stacks are performed in bins of β ($-2.2 < \beta < -1.5$, $-1.5 < \beta < -1.0$, $-1.0 < \beta < -0.5$, $-0.5 < \beta < 0.0$, $0.0 < \beta < 0.5$, $0.5 < \beta < 1.0$, $1.0 < \beta < 1.5$). Three relations are also shown: the relation of local starburst galaxies (solid line; Meurer et al. 1999), the updated relation for local galaxies with wider apertures for UV photometry (dashed line; Overzier et al. 2011), and an SMC-like dust attenuation relation (dotted line; e.g. Prevot et al. 1984). At the high-mass end ($M_* > 10^{10}$ M$_\odot$), individual detections and the stacks show that the massive galaxies on the main sequence at this redshift range are consistent with the M99 relation. Starburst galaxies are generally offset and have ~ 0.5 dex larger IRX values than main-sequence galaxies. Less massive galaxies (10^9 M$_\odot < M_* < 10^{10}$ M$_\odot$) are mostly non-detected, and stacks tentatively show lower values in IRX than the M99 relation.

exhibit any different features (such as errors in β and/or L_{UV}) compared to other galaxies. This indicates that the diversity of dust attenuation properties in massive galaxies is rather limited. Nevertheless, massive galaxies with attenuation curves similar to the SMC may still exist. Deeper ALMA data on currently undetected sources will be required to test this.

Our results confirm that for high-redshift, massive galaxies, on average, there is no noticeable evolution of the IRX–β relationship since $z \sim 4.0$ to the present Universe, as already indicated by several

studies (e.g. Bouwens et al. 2016; Koprowski et al. 2018; McLure et al. 2018).

Starburst galaxies (as identified in Section 3.4) generally have large IRX values, on average ~ 0.5 dex above the local relation. This can be expected, as heavily obscured regions together with a small fraction of non-obscured regions ('holes in dust shields') easily deviate from the M99 relation, because their UV and IR fluxes no longer come from same region of a galaxy (see e.g. Popping, Puglisi & Norman 2017; Narayanan et al. 2018).
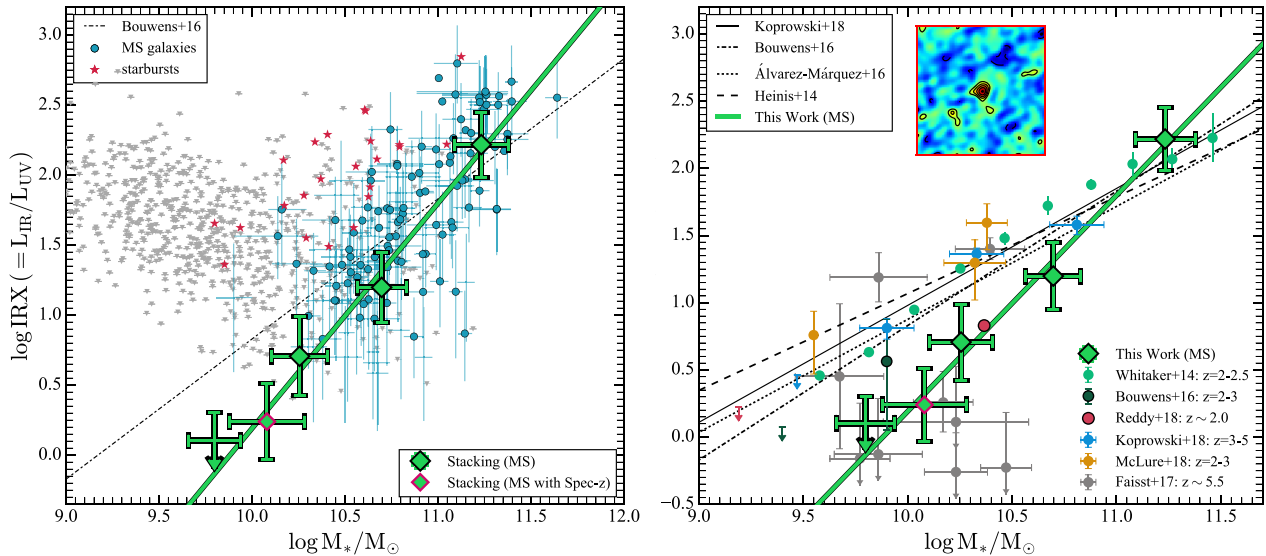
Figure 4. The IRX–M_* diagram of star-forming galaxies at $z = 2.5$–4.0. As in the previous plots, the blue points, red stars, and grey points correspond to main-sequence galaxy detections, starbursts, and 3σ upper limits for non-detections, respectively. Dark green diamonds show our stacking results in bins of mass. The one green diamond with a red edge shows the stacking result for the spectroscopic redshift sample described in Section 4.2.1. The dark green solid line shows our fitting result to the three mass bins at $M_* > 10^{10}$ $M_\odot$. Our measurements reveal a tight correlation between IRX and M_*, with a very steep slope. In the right-hand panel, we compare our results with previous studies at similar redshifts. Interestingly, both our individual detections and the stacks follow a significantly steeper slope of the IRX–M_* relation than previously reported in the literature (e.g. Heinis et al. 2014; Álvarez-Márquez et al. 2016; Bouwens et al. 2016; Koprowski et al. 2018). In particular, our results imply significantly less dust extinction in low-mass galaxies than inferred from previous relations.

4.1.2 IRX–β relation of lower mass galaxies ($M_* < 10^{10}$ $M_\odot$)

For our lower mass sample, we have 970 flux measurements, but only 16 galaxies are detected at $> 3\sigma$. Except for one source, the detected galaxies are all classified as starburst (see Section 3.4). Out of the 970 galaxies, only 80 were the main target of the ALMA observations (typical sensitivity 0.08 mJy beam^{-1}) and the rest only have serendipitous coverage within the primary beam of a neighbouring target. As such, most of the observations were not deep enough to expect an individual detection, in particular, since the lower mass sources ($\log M_*/M_\odot \sim 9.0$–$10.0$) on the main sequence are mostly dominated by blue UV colours ($\beta \lesssim -1.0$), in contrast to their massive counterparts. This trend is seen in Section 3.3, from the β–M_* relationship (see also Fig. 2), which already indicates that lower mass galaxies have a significantly lower dust content than higher mass ones.

As the low-mass galaxies are mostly non-detected, we have to rely on a stacking analysis to provide constraints on the IRX–β relation. However, even when splitting the sample in only two bins of UV slope, we do not find a significant detection in the mean stacked fluxes (see Fig. 3).

For the redder sample, the 3σ upper limit of the stacked flux lies below the M99 relation and is more consistent with SMC dust extinction curve. However, we cannot conclusively rule out the M99 relation, given the IR SED uncertainties. Nevertheless, our result is consistent with the study using deep ALMA band 6 continuum in the Hubble Ultra Deep Field (Bouwens et al. 2016), showing that the stacks of low-mass galaxies ($M_* < 10^{9.75}$ $M_\odot$) typically lie below the IRX–β relation inferred from an SMC-like dust extinction curve. Deeper observations of low-mass galaxies at these redshifts will be required to confirm this.

Theoretically, this mass-dependent difference is predicted from some cosmological hydrodynamical simulations. In particular, Mancini et al. (2015) find that their simulated lower mass galaxies

at $z > 5$ follow an SMC-like dust extinction, while massive galaxies follow the local relation of M99. Our observations indicate that this trend may already be in place at $z \sim 3$–4.

4.2 IRX–M_* relation

In the left panel of Fig. 4, we show the IRX–M_* diagram of our sample. The individual ALMA detections among our main-sequence sample show a relatively tight correlation between IRX and M_*. As expected, starburst galaxies are located above the relation of main-sequence galaxies, indicating that they are more dust extinct at a fixed stellar mass.

In general, the individually detected MS galaxies are in good agreement with the 'consensus relationship' derived in Bouwens et al. (2016) based on several previous studies at $z > 2$. However, we see an indication for a steeper IRX–M_* relation, as the majority of the most massive galaxies lie above the previous relation, while intermediate-mass galaxies ($M_* \sim 10^{10.5}$ $M_\odot$) seem to have lower IRX than the 'consensus relationship' and previous works (e.g. Heinis et al. 2014; Whitaker et al. 2014; Álvarez-Márquez et al. 2016; Bouwens et al. 2016; McLure et al. 2018).

The finding of a significantly steeper IRX–M_* becomes very clear when stacking our full galaxy sample in bins of stellar mass, including non-detections. The results of our stacking analysis at $M_* > 10^{9.5}$ $M_\odot$ are listed in Table 1 and shown in Fig. 4. In particular, at $M_* < 10^{10}$ $M_\odot$, even our stack of more than 300 galaxies did not reveal a detection, indicating a significantly lower IRX value than expected from previous relations, by $\gtrsim 0.5$ dex.

The linear fit to the detected stacked data points (the first three green diamonds) results in the following equation for the IRX–M_* relation:

$$\log \text{IRX} = (1.64 \pm 0.13) \times \log M_* - (16.18 \pm 1.35 \pm 0.2), \quad (4)$$

where M_* is in units of $M_\odot$ and the ± 0.2 dex uncertainty comes from the IR SED shape. This fit is also shown in Fig. 4.

4.2.1 Confirmation from a spectroscopic redshift sample at $z \sim 3.5$

In order to examine if our IRX–β relation might be affected by photometric redshift uncertainties or whether our aperture stacking method might be biased, we have used an alternative stacking method on a sample with redshifts confirmed through spectroscopic observations. The programme we used is 2015.1.00379.S (PI: E. Schinnerer). The sample has redshift measurements from the VUDS spectroscopic survey (Le Fèvre et al. 2015), and is observed with ALMA band 6 (at $\nu_{obs} \sim 240\,GHz$). The sample includes 61 galaxies ranging in stellar mass between $10^{9.5}\,M_\odot < M_* < 10^{10.5}\,M_\odot$ (median M_* of $10^{10.1}\,M_\odot$) with spectroscopic redshifts ranging from 3.0 to 4.74 (median redshift of $z = 3.44$). Using this sample, we employed a stacking method in the visibility domain, as described in Lindroos et al. (2015).

The stacked image shows a 6.1σ detection in the FIR continuum emission, with a flux density of $56 \pm 9\,\mu Jy\,beam^{-1}$, consistent with the value obtained by our stack employing aperture flux averages. The stacked image is shown as an inset in the right-hand panel of Fig. 4. The UV slope, IR luminosity, and UV luminosity are calculated using the same method as described in Section 3.

This stacking result is perfectly consistent with the IRX–M_* relation inferred from individually detected galaxies and from stacks of our entire sample. This confirms that our finding of a steep IRX–mass relation is robust and is neither due to photometric redshift uncertainties nor due to our stacking method.

4.2.2 Comparison with IRX–M_* relations from previous analyses

In the right-hand panel of Fig. 4, we compare our findings with several results in the literature. These include stacking analyses of single-dish sub-mm telescope data, *Spitzer* MIPS, and/or *Herschel* SPIRE data using rest-frame UV/Optical galaxy selections (Heinis et al. 2014; Álvarez-Márquez et al. 2016; Whitaker et al. 2017; Koprowski et al. 2018; Reddy et al. 2018). Additionally, we show the stacking results of ALMA data (Bouwens et al. 2016; McLure et al. 2018), which utilize a smaller field of view, but have a higher angular resolution than the previous observations.

A few of the previous studies are consistent with our finding of a very steep IRX–M_* relation (Bouwens et al. 2016; Reddy et al. 2018). However, most studies report a shallower slope, such that they find higher IRX values for lower mass galaxies (i.e. log$M_* <$ 10.5) (Heinis et al. 2014; Whitaker et al. 2014; Álvarez-Márquez et al. 2016; Koprowski et al. 2018; McLure et al. 2018).

Interestingly, our result of a lower IRX for log $M_*/M_\odot \simeq 10$ galaxies is consistent with the few measurements that currently exist for $z \sim 5$–6 galaxies (Capak et al. 2015; Faisst et al. 2017). In fact, many of the galaxies at those redshifts show log IRX < 0 and are currently undetected in ALMA. Together with our results, this may indicate a possible evolution of the dust properties at $z > 2$, before the peak of the cosmic SFH. We will analyse this in detail in a future paper.

4.2.3 Potential biases of IRX measurements

The origin for the differences with respect to previous measurements is not immediately clear. However, there are several assumptions and biases that can possibly affect both previous studies as well as ours. The most obvious ones, which we discuss in the following are (1) the dust continuum SED shape and (2) potential measurement biases in stacking of low-resolution data (e.g. Herschel).

(1) *Biases due to different FIR SEDs:* The assumed shape of the FIR SED clearly affects the IR luminosity estimates, in particular, if the SED shape changes with stellar mass or luminosity. Our study relies on mm/sub-mm observations of dust continuum emission, which is in the Rayleigh–Jeans regime of the FIR SED from high-redshift galaxies. Thus, mm/sub-mm observations could be biased towards emission from low-temperature dust. If the dominant part of the FIR emission of $z \sim 3$ galaxies arises from higher temperature dust, our L_{IR} (thus IRX) estimation of individual or stacked data could be systematically lower than the intrinsic distribution of L_{IR} and IRX at $z \sim 3$ (see also Ferrara et al. 2017; Liang et al. 2019; Ma et al. 2019 for theoretical predictions of dust temperature at high redshift).

As seen in the Fig. 4, while our IRX measurements agree very well with previous studies for high-mass galaxies, we find a decrement of ~ 0.5 dex for lower mass sources. Most of the previous analyses rely on stacking of shorter wavelength data than what we have access to here, i.e. they can potentially probe wavelengths closer to the peak of the SED. While our assumed template SED was derived through one of the stacks (Álvarez-Márquez et al. 2016) and it is consistent with dust temperature measurements of massive galaxies at these redshifts ($T_d = 40\,K$; e.g. Fudamoto et al. 2017; Schreiber et al. 2018), it is of course possible that the dust temperature and thus the SED shape changes systematically with galaxy mass. In order to flatten our IRX–mass relation, a higher dust temperature would be required for lower mass or lower IR luminous galaxies [i.e. $T_d > 50\,K$ in $\log(M_*/M_\odot) < 10.5$ galaxies]. However, no significant evidence for such trends currently exists from *Herschel* stacks at these redshifts (Schreiber et al. 2018), and lower redshift galaxies seem to show the opposite trend (e.g. Casey et al. 2018a). The variation of dust temperature also affects dust mass estimations, as the inferred dust mass is inversely proportional to the temperature (e.g. Scoville et al. 2016). Therefore, an uncertain dust temperature variation results in an additional systematic uncertainty in the molecular gas mass estimation based on dust masses (Schinnerer et al. 2016; Scoville et al. 2016). It is clear that a direct study of the dust temperature of high-redshift galaxies is crucial to fully understand their FIR emission and to resolve these discrepancies.

(2) *Clustering biases in stacking analyses*: In contrast to our relatively high-resolution ALMA measurements of individual sources, previous studies have mostly relied on stacking of very low-resolution data, which can be significantly affected by clustering biases (see Magnelli et al. 2014; Béthermin et al. 2015). When attempting to stack the *Herschel* fluxes of our galaxies (see the Appendix), it became clear that this clustering bias can become large and difficult to correct for, in particular for low-mass, low-luminosity galaxies. It therefore seems very difficult to make further progress in resolving this issue with current data.

5 CONCLUSIONS

We have analysed the IRX–β/M_* dust attenuation relations of star-forming galaxies at $z \sim 2.5$–4.0 using all the publicly available ALMA archival data in the COSMOS field. In particular, we include all primary targeted galaxies as well as serendipitously covered sources within the primary beamwidth of existing ALMA continuum images that were processed by the A3COSMOS project

team (Liu et al. 2019). The ALMA data were cross-matched with the COSMOS2015 optical–NIR photometric catalogue (Laigle et al. 2016). Our final sample consists of 1510 ALMA flux measurements with beam size 0.5–1.8 arcsec and a typical sensitivity of 126 μJy beam^{-1}. In total, only ~ 10 per cent of the $z \sim 2.5$–4.0 sample is detected with signal-to-noise ratio > 3. The detection rate is highly mass-dependent and decreases significantly below a stellar mass log $(M_*/M_\odot) \sim 10.5$ (Fig. 1).

The analysis of these data leads to the following conclusions:

(i) For massive galaxies with stellar mass greater than $10^{10} M_\odot$, the IRX–β relation is in very good agreement with the local relation derived by Meurer et al. (1999) over a wide range of the UV slope β ($\beta \sim -1.7$ to 1.0). The scatter around the mean relation is small, only 0.27 dex. This indicates that the dust properties do not evolve significantly for massive galaxies between $z \sim 4.0$ and the present-day Universe. This trend is also consistent with the theoretical prediction of hydrodynamic simulations in previous works (e.g. Mancini et al. 2015).

(ii) The detection rate drastically decreases in less-massive galaxies, and individual objects and stacking analyses only provide upper limits on the flux measurements. For galaxies with $M_* < 10^{10} M_\odot$, upper limits on their average IRX values fall below the local relation and are more consistent with an SMC dust attenuation relation. This is consistent with previous, deep ALMA surveys (e.g. Bouwens et al. 2016). However, some tension exists with other works in the literature. For instance, McLure et al. (2018) find that galaxies with even lower mass ($M_* \sim 10^{9.5} M_\odot$) at these redshifts still follow the local IRX–β relation quite well. Deeper data on a larger sample of low-mass galaxies are needed to distinguish between these two findings.

(iii) Our sample shows a tight correlation between IRX and galaxy stellar mass. The slope is found to be steeper than reported in previous analyses which were mostly based on stacks of lower angular resolution data (e.g. *Herschel*) or based on smaller samples. This steep slope implies that $z \sim 3$–4 galaxies with masses below $M_* < 10^{10} M_\odot$ suffer $3\times$ less dust extinction at a given UV luminosity than previous results might have implied. These low extinction values are consistent with early results from small sample of $z \sim 5.5$ galaxies and they could be a first hint at a possible evolution of the dust extinction properties in the early Universe, at $z > 2$, compared to later cosmic times.

(iv) Our results highlight the need of detailed studies on the FIR continuum emission of high-redshift galaxies. In particular, our analysis is based only on the mm/sub-mm ALMA fluxes, from which we derive an estimate of the galaxies' infrared luminosities. Systematic changes of the dust temperature or SED shapes as a function of stellar mass could affect the slope of our inferred IRX–mass relation. To address these possible systematic biases in the future, the FIR SEDs of high-redshift galaxies will need to be studied carefully through direct observations of individual sources at higher frequency (e.g. ALMA band 8/9/10), or through indirect inferences from their local analogues.

ACKNOWLEDGEMENTS

REFERENCES

Arnouts S. et al., 2002, MNRAS, 329, 355
Béthermin M. et al., 2015, A&A, 573, A113
Bouwens R. J. et al., 2014, ApJ, 795, 126
Bouwens R. J. et al., 2016, ApJ, 833, 72
Bruzual G., Charlot S., 2003, MNRAS, 344, 1000
Buat V. et al., 2005, ApJ, 619, L51
Calzetti D., 2001, PASP, 113, 1449
Capak P. L. et al., 2015, Nature, 522, 455
Casey C. M. et al., 2014, ApJ, 796, 95
Casey C. M. et al., 2018a, ApJ, 862, 77
Casey C. M., Hodge J., Zavala J. A., Spilker J., da Cunha E., Staguhn J.,
    Finkelstein S. L., Drew P., 2018b, ApJ, 862, 78
Chabrier G., 2003, PASP, 115, 763
Civano F. et al., 2016, ApJ, 819, 62
Condon J. J., 1997, PASP, 109, 166
Daddi E. et al., 2007, ApJ, 670, 156
Dale D. A., Helou G., 2002, ApJ, 576, 159
Dale D. A., Helou G., Magdis G. E., Armus L., Díaz-Santos T., Shi Y., 2014,
    ApJ, 784, 83
Donley J. L. et al., 2012, ApJ, 748, 142
Dunlop J. S. et al., 2017, MNRAS, 466, 861
Elbaz D. et al., 2007, A&A, 468, 33
Ellis R. S. et al., 2013, ApJ, 763, L7
Faisst A. L. et al., 2017, ApJ, 847, 21
Ferrara A., Hirashita H., Ouchi M., Fujimoto S., 2017, MNRAS, 471, 5018
Finkelstein S. L. et al., 2015, ApJ, 814, 95
Fudamoto Y. et al., 2017, MNRAS, 472, 483
Gordon K. D., Clayton G. C., Witt A. N., Misselt K. A., 2000, ApJ, 533,
    236
Gordon K. D., Clayton G. C., Misselt K. A., Landolt A. U., Wolff M. J.,
    2003, ApJ, 594, 279
Grasha K., Calzetti D., Andrews J. E., Lee J. C., Dale D. A., 2013, ApJ,
    773, 174
Hatziminaoglou E. et al., 2010, A&A, 518, L33
Heinis S. et al., 2013, MNRAS, 429, 1113
Heinis S. et al., 2014, MNRAS, 437, 1268
Ilbert O. et al., 2006, A&A, 457, 841
Ilbert O. et al., 2010, ApJ, 709, 644
Kawamata R., Ishigaki M., Shimasaku K., Oguri M., Ouchi M., 2015, ApJ,
    804, 103
Kennicutt R. C., Jr, 1998, ARA&A, 36, 189
Kinney A. L., Bohlin R. C., Calzetti D., Panagia N., Wyse R. F. G., 1993,
    ApJS, 86, 5
Koekemoer A. M. et al., 2007, ApJS, 172, 196
Kong X., Charlot S., Brinchmann J., Fall S. M., 2004, MNRAS, 349, 769
Koprowski M. P. et al., 2018, MNRAS, 479, 4355
Laigle C. et al., 2016, ApJS, 224, 24
Laporte N. et al., 2016, ApJ, 820, 98
Le Borgne D., Elbaz D., Ocvirk P., Pichon C., 2009, A&A, 504, 727
Le Fèvre O. et al., 2015, A&A, 576, A79
Liang L. et al., 2019, MNRAS, 489, 1397
Lindroos L., Knudsen K. K., Vlemmings W., Conway J., Martí-Vidal I.,
    2015, MNRAS, 446, 3502
Liu D. et al., 2019, ApJS, 244, 40
Ma X. et al., 2019, MNRAS, 487, 1844
Madau P., Dickinson M., 2014, ARA&A, 52, 415
Magdis G. E. et al., 2012, ApJ, 760, 6
Magnelli B. et al., 2013, A&A, 553, A132
Magnelli B. et al., 2014, A&A, 561, A86
Mancini M., Schneider R., Graziani L., Valiante R., Dayal P., Maio U.,
    Ciardi B., Hunt L. K., 2015, MNRAS, 451, L70
McCracken H. J. et al., 2012, A&A, 544, A156
McLeod D. J., McLure R. J., Dunlop J. S., 2016, MNRAS, 459, 3812
McLure R. J. et al., 2013, MNRAS, 432, 2696
McLure R. J. et al., 2018, MNRAS, 476, 3991
McMullin J. P., Waters B., Schiebel D., Young W., Golap K., 2007, in Shaw
    R. A., Hill F., Bell D. J., eds, ASP Conf. Ser. Vol. 376, Astronomical Data

Analysis Software and Systems XVI. Astron. Soc. Pac., San Francisco,
    p. 127
Meurer G. R., Heckman T. M., Calzetti D., 1999, ApJ, 521, 64(M99)
Narayanan D., Davé R., Johnson B. D., Thompson R., Conroy C., Geach J.,
    2018, MNRAS, 474, 1718
Noeske K. G. et al., 2007, ApJ, 660, L43
Oesch P. A. et al., 2010, ApJ, 714, L47
Oesch P. A., Bouwens R. J., Illingworth G. D., Franx M., Ammons
    S. M., van Dokkum P. G., Trenti M., Labbé I., 2015, ApJ, 808,
    104
Oesch P. A., Bouwens R. J., Illingworth G. D., Labbé I., Stefanon M., 2018,
    ApJ, 855, 105
Overzier R. A. et al., 2011, ApJ, 726, L7
Pannella M. et al., 2015, ApJ, 807, 141
Peng C. Y., 2002, AJ, 124, 294
Peng C. Y., Ho L. C., Impey C. D., Rix H.-W., 2010, AJ, 139, 2097
Popping G., Puglisi A., Norman C. A., 2017, MNRAS, 472, 2315
Prevot M. L., Lequeux J., Maurice E., Prevot L., Rocca-Volmerange B.,
    1984, A&A, 132, 389
Qin J., Zheng X. Z., Wuyts S., Pan Z., Ren J., 2019, MNRAS, 485, 5733
Reddy N. et al., 2012, ApJ, 744, 154
Reddy N. A., Erb D. K., Pettini M., Steidel C. C., Shapley A. E., 2010, ApJ,
    712, 1070
Reddy N. A. et al., 2018, ApJ, 853, 56
Salim S., Boquien M., 2018, ApJ, 859, 11
Salim S. et al., 2007, ApJS, 173, 267
Salpeter E. E., 1955, ApJ, 121, 161
Scalo J. M., Slavsky D. B., 1980, ApJ, 239, L73
Schenker M. A. et al., 2013, ApJ, 768, 196
Schinnerer E. et al., 2016, ApJ, 833, 112
Schreiber C. et al., 2015, A&A, 575, A74
Schreiber C., Elbaz D., Pannella M., Ciesla L., Wang T., Franco M., 2018,
    A&A, 609, A30
Scoville N. et al., 2007, ApJS, 172, 1
Scoville N. et al., 2016, ApJ, 820, 83
Takeuchi T. T., Buat V., Heinis S., Giovannoli E., Yuan F.-T., Iglesias-Páramo
    J., Murata K. L., Burgarella D., 2010, A&A, 514, A4
Takeuchi T. T., Yuan F.-T., Ikeyama A., Murata K. L., Inoue A. K., 2012,
    ApJ, 755, 144
Whitaker K. E., van Dokkum P. G., Brammer G., Franx M., 2012, ApJ, 754,
    L29
Whitaker K. E. et al., 2014, ApJ, 795, 104
Whitaker K. E., Pope A., Cybulski R., Casey C. M., Popping G., Yun M. S.,
    2017, ApJ, 850, 208
Zavala J. A., Casey C. M., da Cunha E., Spilker J., Staguhn J., Hodge J.,
    Drew P. M., 2018, ApJ, 869, 71
Álvarez-Márquez J. et al., 2016, A&A, 587, A122
Álvarez-Márquez J., Burgarella D., Buat V., Ilbert O., Pérez-González P. G.,
    2019, A&A, 630, A153

APPENDIX: COMPARISON OF SED TEMPLATES

In Section 4.2, we computed the IRX–M_* relation from our A3COSMOS sample, and compared it to several previous results. We have found that our IRX–M_* relation is significantly steeper, such that galaxies with stellar mass of $M_* < 10^{10}\,\mathrm{M_\odot}$ show lower values of IRX than obtained by previous studies.

However, as pointed out in the text, the shape of the IR SED can significantly affect the inferred L_{IR}. Here, we thus investigate the potential effect of using different SEDs. In Fig. A1, we plot representative SED templates used in previous studies that are publicly available, and compare it to our baseline SED model. This includes SEDs used in Heinis et al. (2013), Whitaker et al. (2014), Álvarez-Márquez et al. (2016), and Casey et al. (2018b). For each template, we calculate L_{IR} by integrating over 8–1000 μm
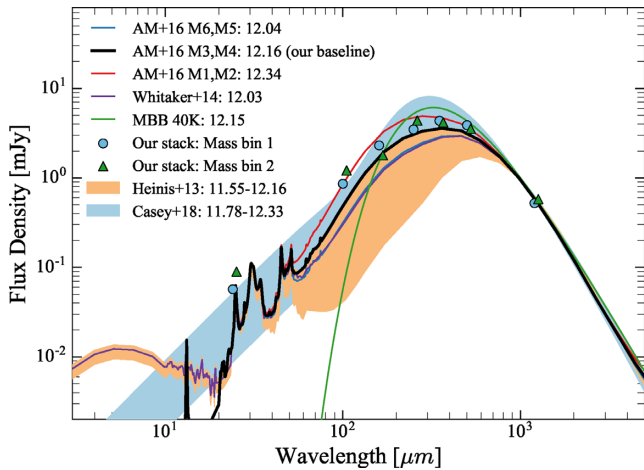
Figure A1. Comparison of the IR SED templates used in several previous studies (Heinis et al. 2013; Whitaker et al. 2014; Álvarez-Márquez et al. 2016; Casey et al. 2018b). All templates here are normalized to have 1 mJy, after redshifting to $z = 3.0$. For Álvarez-Márquez et al. (2016, denoted as AM + 16), we plot the three different SED models for the stellar mass ranges $\log(M_*/M_\odot) = 9.75$–10.25 (M1, M2 model), $\log(M_*/M_\odot) = 9.25$–10.75 (M3, M4 model), and $\log(M_*/M_\odot) = 10.75$–11.25 (M5, M6 model). In the upper left legend, we report the IR luminosities obtained from each of the normalized templates in units of $\log(L_{IR}/L_\odot)$. The green solid line indicates an optically thin modified blackbody SED with dust temperature of 40 K. Most SEDs result in an inferred $\log(L_{IR}/L_\odot) = 12.1 \pm 0.2$; however, there are clearly systematic differences between models. For the current work, we adopt a fixed baseline SED: the AM + 16 model at $\log(M_*/M_\odot) = 9.25$–10.75, and we add a 0.2 dex systematic uncertainty to all our reported values. For comparison, the stacked *Herschel* fluxes for two mass bins of our sample are plotted as triangles [$\log(M_*/M_\odot) = 10.5$–11] and circles [$\log(M_*/M_\odot) = 11$–12] after clustering correction, as described in Magnelli et al. (2014), and after normalizing fluxes to match the shown SEDs.

after normalizing all SED templates to 1 mJy at 1000 μm (i.e. the typical wavelength of our ALMA measurements).

As shown in Fig. A1, the L_{IR} of our assumed SED template agrees well with that of several other templates within a typical systematic difference of ~ 0.2 dex. In principle, this difference in the bolometric correction depends slightly on the wavelength that is used to normalize. However, the changes are small and do not affect our conclusion.

In Heinis et al. (2013), Whitaker et al. (2014), and Álvarez-Márquez et al. (2016), the authors utilize FIR SED models from Dale & Helou (2002), Dale et al. (2014), or log averages of Dale & Helou (2002). These SED templates are used to obtain bolometric corrections from stacked 24 μm fluxes (Whitaker et al. 2014), or to determine the best-fitting templates to the stacked 250–850 μm

photometry (Heinis et al. 2013; Álvarez-Márquez et al. 2016). In Álvarez-Márquez et al. (2016), galaxies are stacked by splitting the sample in six stellar mass bins ($\log(M_*/M_\odot) = 9.75$–11.25 with $\delta\log(M_*/M_\odot) = 0.25$), which resulted in three different SED models. Recall that we use the middle one of these templates appropriate for $\log(M_*/M_\odot) = 10$ as our baseline SED. As shown in the figure, most of these SEDs result in similar L_{IR} values when normalized to the ALMA flux measurement, with the exception of the templates used in Heinis et al. (2013), which are somewhat shifted to lower values by up to 0.5 dex.

In Casey et al. (2018b), the authors utilize an analytic formula that represents the mid- to far-IR emission of local IR luminous galaxies combining an optically thick modified blackbody and a mid-IR power-law component. Additionally, the authors implemented a relationship between L_{IR} and peak wavelength (λ_{peak}) to derive their SEDs (equation 2 of Casey et al. 2018a). In order to compare to this model, we choose SEDs that have λ_{peak} corresponding to the range of L_{IR} of our sample (i.e. $L_{IR}/L_\odot = 10^{10}$–10^{13}). This large range of SED shapes results in a difference of inferred $\log L_{IR}$ of more than 0.5 dex, when normalized to our observed ALMA fluxes. However, the range again spans the $\log L_{IR}$ of our baseline SED within $\sim\pm 0.2$ dex. Interestingly, using the Casey et al. (2018a) SED model for our analysis would further steepen the IRX–M_* relation, because λ_{peak} is set to be inversely proportional to L_{IR}, resulting in lower dust temperatures at lower IR luminosity or in less massive galaxies. However, for simplicity, we use a fixed SED for all galaxies in the main text. Future observations will be required to test for possible changes in SED shapes with galaxy properties at these redshifts.

The validity of our baseline SED is, however, confirmed by stacks of far-IR fluxes from our galaxy sample. In particular, we performed a stacking analysis of the *Herschel* images in two different mass bins using the same method and clustering correction as in Magnelli et al. (2014). In Fig. A1, we show the results for the two highest mass bins, $\log(M_*/M_\odot) = 10.5$–11 and $\log(M_*/M_\odot) = 11$–12, for which the *Herschel* fluxes were well-detected and for which the correction factor for clustering were of order ~ 1.2–1.6 (see Magnelli et al. 2014; Béthermin et al. 2015). For the purpose of this plot, the stacked fluxes were renormalized to fit the plotted SEDs. As can be seen, the shape of our baseline FIR SED is well-matched to the observed fluxes.

The above analysis suggest that the use of our baseline SED template from Álvarez-Márquez et al. (2016) is well-justified and that our derived L_{IR} values are consistent with a range of different SED models within a systematic uncertainty of $\sim\pm 0.2$ dex, which we add to our derived values in the main text of the paper.

This paper has been typeset from a TₑX/LATₑX file prepared by the author.